Journal of Materials Chemistry C

ROYAL SOCIETY OF CHEMISTRY

PAPER

View Article Online
View Journal | View Issue



Cite this: J. Mater. Chem. C, 2022, 10, 15061

# A theoretical study of the *Pnma* and $R\bar{3}m$ phases of $Sb_2S_3$, $Bi_2S_3$, and $Sb_2Se_3$

E. Lora da Silva, *[a] J. M. Skelton, [b] P. Rodríguez-Hernández, [c] A. Muñoz, [c] M. C. Santos,[de] D. Martínez-García,[f] R. Vilaplana [g] and F. J. Manjón [e]

Received 11th April 2022,
Accepted 28th July 2022

DOI: 10.1039/d2tc01484j

rsc.li/materials-c

We report a comparative theoretical study of the *Pnma* and $R\bar{3}m$ phases of $Sb_2S_3$, $Bi_2S_3$, and $Sb_2Se_3$ close to ambient pressure. Our enthalpy calculations at 0 K show that at ambient pressure the $R\bar{3}m$ (tetradymite-like) phase of $Sb_2Se_3$ is energetically more stable than the *Pnma* phase, contrary to what is observed for $Sb_2S_3$ and $Bi_2S_3$, and irrespective of the exchange–correlation functional employed in the calculations. The result for $Sb_2Se_3$ is in contradiction to experiments in which all three compounds are usually grown in the *Pnma* phase. This result is further confirmed by free-energy calculations taking into account the temperature dependence of unit-cell volumes and phonon frequencies. Lattice dynamics and elastic tensor calculations further show that both the *Pnma* and $R\bar{3}m$ phases of $Sb_2Se_3$ are dynamically and mechanically stable at zero applied pressure. Since these results suggest that the formation of the $R\bar{3}m$ phase of $Sb_2Se_3$ should be feasible under close to ambient conditions, we provide a theoretical crystal structure and simulated Raman and infrared spectra to help in its identification. We also discuss the results of the two published works that have claimed to have synthesized tetradymite-like $Sb_2Se_3$. Finally, the stability of the $R\bar{3}m$ phase across the three group-15 $A_2X_3$ sesquichalcogenides is analysed based on their van der Waals gap and X–X in-plane geometry.



## 1 Introduction

Since the identification of the trigonal tetradymite-like $R\bar{3}m$ phases of group-15 sesquichalcogenides (*i.e.* $Sb_2Te_3$, $Bi_2Se_3$, and $Bi_2Te_3$; Fig. 1a) as 3D topological insulators,[1,2] the family of $A_2X_3$ sesquichalcogenides has attracted a great deal of attention from the scientific community. Three-dimensional topological insulators represent a new class of matter, with insulating bulk electronic states and topologically protected metallic surface states arising from time-reversal symmetry and strong spin–orbit coupling (SoC). These properties make them of potential interest for spintronics and quantum computing applications.[3] Due to this fundamental interest and potential applications, the identification of new topological insulators and materials with superconducting properties is currently an important research area in condensed matter science.

The stibnite ($Sb_2S_3$), bismuthinite ($Bi_2S_3$), and antimonselite ($Sb_2Se_3$) minerals are also group-15 sesquichalcogenides but do not crystallize in the tetradymite-like $R\bar{3}m$ structure under ambient conditions and instead are reported to adopt an orthorhombic $U_2S_3$-type *Pnma* structure (Fig. 1b). $Sb_2S_3$, $Bi_2S_3$, and $Sb_2Se_3$ are semiconductors with band gap widths of 1.7, 1.3, and 1.2 eV, respectively.[4,5] These materials are used in a wide range of technological applications including photovoltaics (solar cells), X-ray computed tomography detectors, fuel cells, gas sensors, and for the detection of biomolecules.[6–12] Additionally, $Sb_2Se_3$ has recently found a number of other applications including in solid-state batteries, fiber lasers, and photoelectrochemical devices.[13–16]

Since several phases, including the *Pnma* phase, have been synthesized for $Bi_2Se_3$, which usually crystallizes in the tetradymite-like $R\bar{3}m$ structure,[17–20] it is natural to wonder whether the $R\bar{3}m$ structure could be adopted by other sesquichalcogenides that generally adopt the $U_2S_3$-type structure, *viz.* $Sb_2S_3$, $Bi_2S_3$, and in particular $Sb_2Se_3$. In fact, several theoretical studies have been performed over the years to investigate the properties of the hypothetical tetradymite-like $Sb_2Se_3$ structure. Some of these studies have suggested that this phase should undergo a topological quantum phase transition under

[a] IFIMUP, Departamento de Física e Astronomia, Faculdade de Ciências da Universidade do Porto, 4169-007, Porto, Portugal. E-mail: estelina.silva@fc.up.pt; Fax: +351 22 04 02 406; Tel: +351 22 04 02 362
[b] Department of Chemistry, University of Manchester, Oxford Road, Manchester, M13 9PL, UK
[c] Departamento de Física, Instituto de Materiales y Nanotecnología, MALTA Consolider Team, Universidad de La Laguna, 38206, Tenerife, Spain
[d] Sede do Agrupamento Escolas de Ponte de Sor, 7400-259, Ponte de Sor, Portugal
[e] Instituto de Diseño para la Fabricación y Producción Automatizada, MALTA Consolider Team, Universitat Politècnica de València, 46022, València, Spain
[f] Departamento de Física Aplicada – ICMUV, MALTA Consolider Team, Universitat de València, 46100, Burjassot, Spain
[g] Centro de Tecnologías Físicas, MALTA Consolider Team, Universitat Politècnica de València, 46022, València, Spain

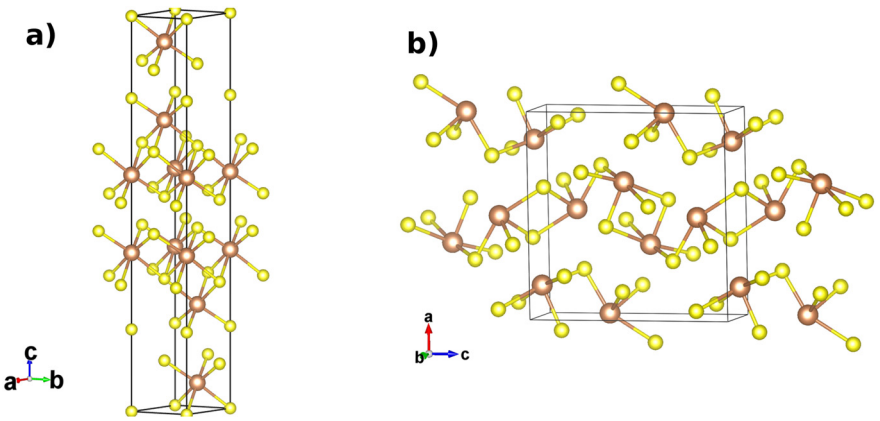


Fig. 1 Structures of the $R\bar{3}m$ (a) and *Pnma* (b) phases of the $A_2X_3$ sesquichalcogenides (A = Sb, Bi and X = S, Se). The A cations and X anions are shown as brown and yellow spheres, respectively.

compression,[21,22] while one found that tetradymite-like $Sb_2Se_3$ is dynamically stable and is a topological insulator at ambient pressure.[23] Interestingly enough, the $R\bar{3}m$ phases of group-15 sesquichalcogenides are characterized by a unique type of bonding termed "metavalent bonding" that not only underpins the topological properties but also makes these materials useful for phase-change memories, as highly efficient thermoelectrics, and for photonic devices.[24]

In 2013 an experimental study claimed to have observed the $R\bar{3}m$ phase of $Sb_2Se_3$, with a topological transition occurring at 2 GPa,[25] but the tetradymite-like structure of $Sb_2Se_3$ was not confirmed beyond doubt. On the other hand, a comparative experimental and theoretical study of the three $U_2S_3$-type sesquichalcogenides suggested the *Pnma* structure to be stable up to 50 GPa.[26] This is supported by several experimental high-pressure studies on $Sb_2Se_3$ in which the *Pnma* structure was found to be stable up to 50 GPa and above.[27,28] However, one study observed a pressure-induced isostructural phase transition at 12 GPa and a further transition to a disordered $Im\bar{3}m$ structure above 50 GPa, followed by a pressure-induced amorphization on releasing the pressure.[29] Despite the apparent stability of the *Pnma* phase, experimental high-pressure studies have also found that *Pnma* $Sb_2Se_3$ becomes a topological superconductor at 2.5 K and around 10 GPa,[30] exhibiting highly conducting spin-polarized surface states similar to those observed for $Bi_2Se_3$.[31] Furthermore, a recent study has claimed to have synthesized $R\bar{3}m$ of $Sb_2Se_3$ by atomic layer epitaxy on a buffer layer of $Bi_2Se_3$.[32] We can therefore conclude that while the bulk of the experimental evidence suggests that the $R\bar{3}m$ phase of $Sb_2Se_3$ is not observed at high pressures, it is not conclusive as to whether this phase could potentially be formed under favourable synthesis conditions.

In light of the above studies, it is interesting to compare the stabilities of the *Pnma* and $R\bar{3}m$ structural phases of the three $U_2S_3$-type sesquichalcogenides under close to ambient conditions and to confirm whether or not the $R\bar{3}m$ phase could be synthetically accessible. In this work, we report a set of systematic density-functional theory (DFT) calculations on the *Pnma* and $R\bar{3}m$ phases of the three $U_2S_3$-type sesquichalcogenides under ambient conditions and at pressures up to 10 GPa. We show that the *Pnma* phases of $Sb_2S_3$ and $Bi_2S_3$ are energetically more stable than the $R\bar{3}m$ phases over this pressure range, but that, unexpectedly, the $R\bar{3}m$ phase of $Sb_2Se_3$ is predicted by several exchange–correlation (XC) functionals to be more stable than the *Pnma* phase close to ambient conditions. To aid in future experimental efforts to prepare the $R\bar{3}m$ phase of $Sb_2Se_3$, we also confirm its dynamical and mechanical stability and provide a theoretical structure and vibrational spectra to support its identification. Finally, we also discuss the only two studies that, to our knowledge, have claimed to have prepared the tetradymite-like phase of $Sb_2Se_3$ under close to ambient conditions.

## 2 Methods

The structural properties of the different crystalline phases of $Sb_2S_3$, $Bi_2S_3$, and $Sb_2Se_3$ were calculated within the framework of pseudopotential plane-wave density-functional theory[33] using the Vienna *Ab initio* Simulation Package (VASP) code.[34] The revised Perdew–Burke–Ernzerhof generalized-gradient approximation (GGA) functional for solids (PBEsol)[35,36] was used for all calculations. Additional calculations were also performed with the local-density approximation (LDA)[37] functional and the dispersion-corrected PBE-D2[38] functional to assess the impact of the XC treatment on the results. Projector augmented-wave (PAW) pseudopotentials including six valence electrons for S[$3s^2$ $3p^4$] and Se[$4s^2$ $4p^4$] and fifteen valence electrons for Sb[$4d^{10}$ $5s^2$ $5p^3$] and Bi[$5d^{10}$ $6s^2$ $6p^3$] were used to model the ion cores. The convergence of the total energy was achieved with a plane-wave kinetic-energy cut-off of 600 eV. The Brillouin zones (BZs) were sampled with Γ-centered Monkhorst-Pack[39] grids with 6 × 10 × 6 (*Pnma*) and 12 × 12 × 12 subdivisions ($R\bar{3}m$).

Structural relaxations were performed by allowing the atomic positions and the unit-cell parameters to optimise at a series of fixed volumes in order to confirm the stability of both the *Pnma* and $R\bar{3}m$ phases over a pressure range from 0–10 GPa. At each volume, we obtain the (hydrostatic) external pressure

 

for the applied compression and the corresponding structural parameters. The pressure–volume ($p$–$V$) curves for each of the compounds were fitted to a third-order Birch–Murnaghan equation of state[40,41] to obtain the equilibrium volume, the bulk modulus, and its pressure derivative. The enthalpy $H$ as a function of volume was computed using the relationship $H = E + pV$, where $E$ is the total electronic energy of the system, $p$ is the pressure, and $V$ is the volume. Comparison of the $H$ curves of the different polymorphs can provide insight into the relative thermodynamic stabilities over the studied pressure range.

Lattice-dynamics calculations were performed on the *Pnma* and $R\bar{3}m$ phases of $Sb_2Se_3$ at a series of cell volumes corresponding to different applied pressures. The phonon frequencies were computed by using the supercell finite-displacement method implemented in the Phonopy package[42] with VASP as the force calculator.[43] Supercell expansions of $2 \times 4 \times 2$ for the *Pnma* phase and $2 \times 2 \times 2$ for the $R\bar{3}m$ phases were used to enable the exact calculation of frequencies at the zone center ($\Gamma$) and unique zone-boundary wave vectors, which were interpolated to obtain phonon-dispersion curves together with density of states curves on uniform $50 \times 50 \times 50$ $\Gamma$-centered $q$-point meshes.

Infrared (IR) and Raman spectra were calculated for the ground-state $R\bar{3}m$ phase of $Sb_2Se_3$ using the methods described in ref. 44 and implemented in the Phonopy-Spectroscopy package.[45] The spectral linewidths were obtained by computing the third-order force constants of a $2 \times 2 \times 2$ expansion of the primitive cell, and following the many-body perturbative approach described in detail in ref. 46 and implemented in the Phono3py software.

Elastic tensors were computed to assess the mechanical stability of the *Pnma* and $R\bar{3}m$ phases of $Sb_2Se_3$ at zero pressure, by employing the central-difference method where the unique components of the elastic tensor are determined by performing six finite distortions of the lattice and deriving the tensor elements from the strain–stress relationship.[47] For these calculations, it was necessary to increase the plane-wave energy cutoff to 950 eV to converge the stress tensor. We then employed the ELATE software[48] to analyze the linear compressibility using the results.

# 3 Results and discussion

## 3.1 Structural properties of the *Pnma* phase

In order to verify the accuracy of our calculations as a prior step before attempting to study the potential $R\bar{3}m$ phases of $Sb_2S_3$, $Bi_2S_3$ and $Sb_2Se_3$, we first calculated the equilibrium lattice parameters, bulk moduli and pressure derivatives of the *Pnma* phases and compared them to other experimental and theoretical studies in the literature (Table 1).

The *Pnma* phases of $A_2X_3$ sesquichalcogenides comprise layers stacked by weak interactions along the crystallographic $a$ direction, the description of which is challenging for conventional DFT functionals.[26,51,63]

Table 1 Calculated equilibrium lattice parameters ($a_0$, $b_0$ and $c_0$), bulk moduli ($B_0$) and pressure derivatives ($B_0'$) of the *Pnma* phases of $Sb_2Se_3$, $Sb_2S_3$ and $Bi_2S_3$ compared to experiments and other theoretical results from the literature

| | $Sb_2Se_3$ | | $Sb_2S_3$ | | $Bi_2S_3$ | |
|---|---|---|---|---|---|---|
| | Theo. | Exp. | Theo. | Exp. | Theo. | Exp. |
| $a_0$ (Å) | 11.75[a] | | 11.24[a] | | 11.19[a] | |
| | 11.80[b] | 11.80[f] | 11.27[b] | 11.30[bjk] | 11.41[b] | 11.27[p] |
| | 11.52[c] | 11.79[g] | 11.02[c] | 11.31[lm] | 11.00[n] | 11.33[q] |
| | 11.91[d] | | 11.30[h] | | 11.58[o] | |
| | 11.53[e] | | 11.08[i] | | | |
| $b_0$ (Å) | 3.98[a] | | 3.83[a] | | 3.96[a] | |
| | 3.99[b] | 3.98[f] | 3.81[c] | 3.84[bjk] | 3.97[b] | 3.97[p] |
| | 3.96[ce] | 3.99[g] | 3.84[h] | 3.84[lm] | 3.94[n] | 3.98[q] |
| | 3.98[d] | | 3.83[bi] | | 3.99[o] | |
| $c_0$ (Å) | 11.30[a] | | 10.91[a] | | 10.94[a] | |
| | 11.28[b] | 11.65[fg] | 10.89[b] | 11.23[bjlm] | 11.01[b] | 11.13[p] |
| | 11.22[ce] | | 10.79[c] | 11.24[k] | 10.83[n] | 11.18[q] |
| | 11.70[d] | | 11.22[h] | | 11.05[o] | |
| | | | 10.81[i] | | | |
| $V_0$ (Å$^3$) | 528.11[a] | | 469.6[a] | | 484.4[a] | |
| | 531.1[b] | 547.1[f] | 470.4[b] | 486.0[b] | 498.3[b] | 498.4[p] |
| | 511.8[c] | 547.5[g] | 453.0[c] | 487.7[imj] | 469.1[n] | 501.6[q] |
| | 598.1[r] | 552.5[s] | 529.9[r] | 488.2[k] | 510.1[o] | |
| | | | | | 511.6[q] | |
| $B_0$ (GPa) | 31.1[a] | | 31.5[a] | | 42.3[a] | |
| | 70.5[c] | 30.0[f] | 32.2[b] | 37.6[b] | 83.6[n] | 36.6[p] |
| | | 32.7[s] | 80.3[c] | 26.9[j] | 32.3[o] | 38.9[q] |
| | | | | 27.2[k] | 36.5[q] | 37.5[u] |
| | | | | 41.4[t] | | |
| $B_0'$ | 6.6[a] | | 6.6[a] | | 6.8[a] | |
| | | 6.1[f] | 6.2[b] | 3.8[b] | 5.9[q] | 6.4[p] |
| | | 5.6[s] | | 7.9[j] | 6.4[o] | 5.5[q] |
| | | | | 6.0[k] | | 4.6[u] |
| | | | | 7.8[t] | | |

[a] This work. [b] Ref. 26. [c] Ref. 49. [d] Ref. 50. [e] Ref. 51. [f] Ref. 27. [g] Ref. 52. [h] Ref. 53. [i] Ref. 54. [j] Ref. 55. [k] Ref. 56. [l] Ref. 57. [m] Ref. 58. [n] Ref. 59. [o] Ref. 60. [p] Ref. 61. [q] Ref. 62. [r] Ref. 63. [s] Ref. 30. [t] Ref. 64. [u] Ref. 65.

The calculated lattice parameters of $Sb_2Se_3$ ($a_0$ = 11.75 Å, $b_0$ = 3.98 Å and $c_0$ = 11.30 Å) are in good agreement with the experimental measurements in ref. 27 and 52 ($a_0$ = 11.80 Å, $b_0$ = 3.97 Å, $c_0$ = 11.65 Å and $a_0$ = 11.79 Å, $b_0$ = 3.98 Å and $c_0$ = 11.65 Å, respectively), and also with other *ab initio* calculations.[26,49–51] The most notable deviation of our calculated values from experimental measurements is a ~3% reduction of the $c_0$ parameter, which contributes to a ~3–4% underestimation of $V_0$ compared to experiments. Our results are comparable to the theoretical results in ref. 26, where calculations were also carried out using PAW pseudopotentials and the PBEsol functional. The $c_0$ of 11.70 Å quoted in ref. 50 is considerably larger than the present results but closer to experiments, but the $a_0$ parameter has a larger error. We attribute this to the use of the PBE functional in this study, which has a tendency to overestimate volumes and has been shown to do so by ~10% for antimony chalcogenides.[63] On the other hand, the LDA tends to underestimate volumes, as can be seen in the lattice parameters quoted in ref. 49, 51 and 59.

Interestingly, the difference in the predicted and measured *b*-axis lengths is very small, which we attribute to the fact that this crystallographic direction corresponds to covalently bonded chains of atoms.

Our calculated lattice parameters for the *Pnma* phase of $Sb_2S_3$ show similar trends to those of $Sb_2Se_3$. As shown in Table 1, the calculated parameters agree well with experimental measurements[26,55] and other theoretical results.[26,49,53,54] We note that, however, for $Sb_2Se_3$, the lattice parameters obtained from LDA calculations tend to underestimate compared to experiments, resulting in discrepancies with the $a_0$ quoted in ref. 49 and 54, although the $c_0$ parameter is closer to our PBEsol results than to the PBE values quoted in ref. 53, which again agree better with experimental results.[26,55]

Our results for $Bi_2S_3$ are also consistent with experimental measurements and other theoretical studies in the literature. We note that calculations performed on $Bi_2S_3$ using the Armiento and Mattsson 2005 parametrized GGA functional (AM05)[66–68] seem to show a slightly better reproduction of the $c_0$ parameter compared to experiments.[26]

The calculated $B_0$ and $B_0'$ values obtained by fitting the *p*–*V* curves of $Sb_2Se_3$ to a third-order Birch–Murnaghan equation are $B_0$ = 31.1 GPa ($B_0'$ = 6.6), which are close to the experimental values of $B_0$ = 30 GPa ($B_0'$ = 6.1) from ref. 27 and $B_0$ = 32.7 GPa ($B_0'$ = 5.6) from ref. 60. For $Sb_2S_3$, we obtained $B_0$ = 31.5 GPa ($B_0'$ = 6.6), which is within the range of experimental values[26,55,56,64] and consistent with the PAW/PBEsol calculations in ref. 26 These results are also close to those experimentally measured for the As-doped stibnite mineral.[69] Finally, our values of $B_0$ = 42.3 GPa ($B_0'$ = 6.8) for $Bi_2S_3$ are again consistent with other DFT calculations[60,62] and the experimental values reported in ref. 61, 62 and 65.

### 3.2 Energetic stability of the *Pnma* and $R\bar{3}m$ phases at 0 K and up to 10 GPa

Since our calculations on the *Pnma* phases were found to be in good agreement with experimental and theoretical studies, we proceeded to carry out a theoretical study of the potential $R\bar{3}m$ phases of $Sb_2S_3$, $Bi_2S_3$, and $Sb_2Se_3$ to probe whether this phase could be energetically competitive from ambient pressure up to 10 GPa.

Fig. 2a–c show the pressure dependence of the enthalpy differences between the $R\bar{3}m$ and *Pnma* phases of $Sb_2S_3$, $Bi_2S_3$, and $Sb_2Se_3$, respectively. We found that the orthorhombic *Pnma* phase is the most energetically stable phase of $Bi_2S_3$ and $Sb_2S_3$ at all the pressures examined, as expected from experiments that obtained this phase both under ambient conditions and at high pressures. Surprisingly, however, our simulations predict that the $R\bar{3}m$ phase of $Sb_2Se_3$ is more stable than the *Pnma* phase below 4.8 GPa, indicating that both the *Pnma* and $R\bar{3}m$ phases are energetically competitive over this range. This in principle contradicts existing experimental studies on $Sb_2Se_3$ that have so far consistently obtained the *Pnma* phase under ambient conditions. We note, however, that the energy difference between the two phases is only 22.71 meV per f.u., which is lower than $k_BT \approx 25$ meV at 300 K and which should therefore make it accessible under ambient conditions.

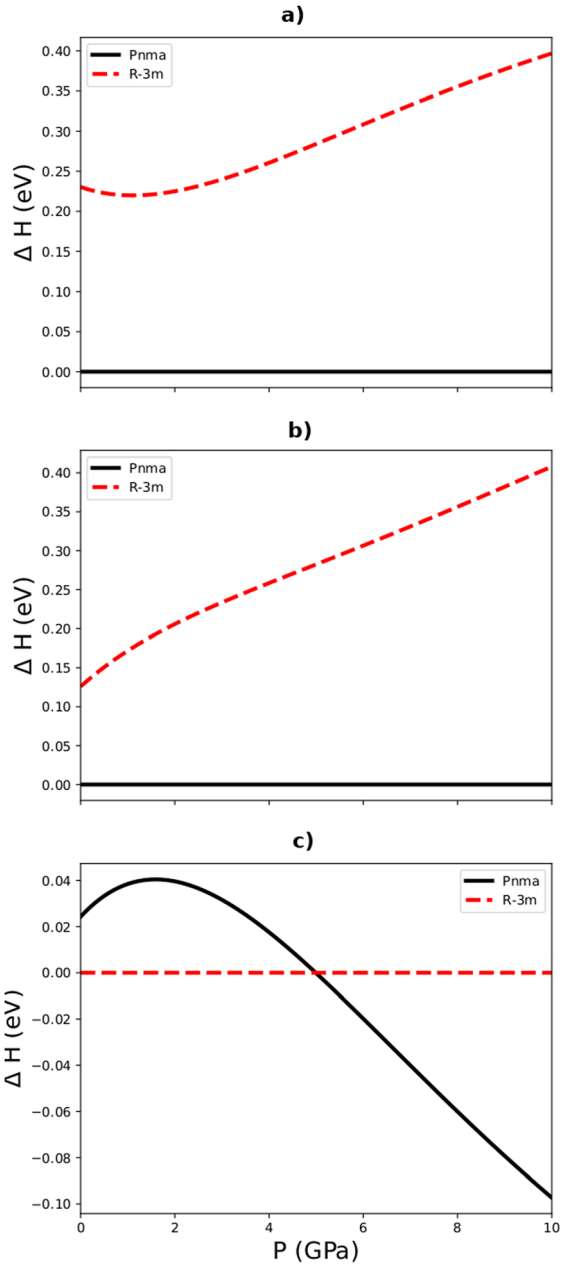


Fig. 2 Calculated relative enthalpy *vs.* pressure up to 10 GPa for the *Pnma* and *R*3*m* phases (*c.f.* Fig. 1) of $Sb_2S_3$ (a), $Bi_2S_3$ (b), and $Sb_2Se_3$ (c) relative to the predicted lowest-energy phase at ambient pressure, *viz.* the *Pnma* phases of $Sb_2S_3$ and $Bi_2S_3$ and the $R\bar{3}m$ phase of $Sb_2Se_3$.

In order to rule out the possibility that these results could be due to inaccuracies with the PBEsol XC functional, we also computed the enthalpies of the two phases with two additional functionals, namely the LDA[37] and the PBE-D2 method.[38] The results of these calculations are presented as an Appendix (Section 5.1). The unit-cell volumes of the *Pnma* phases obtained with the two functionals are underestimated and overestimated with respect to the PBEsol results shown in

 

Table 1, as expected. For PBEsol, the two additional functionals predict that at ambient pressure the $R\bar{3}m$ phase of $Sb_2Se_3$ is more energetically stable than the *Pnma* phase, and remains so up to ~6 GPa (LDA) and 8 GPa (PBE-D2). On the other hand, both functionals predict that the *Pnma* phases of $Sb_2S_3$ and $Bi_2S_3$ are more stable than the $R\bar{3}m$ phase up to at least 10 GPa.

For the $Sb_2Se_3$ structure, we have also investigated the effect of SoC on the energy differences between the two phases. With SoC, the $R\bar{3}m$ phase is also predicted to be more stable than the *Pnma* phase with an energy difference of around 27.38 meV per f.u., a difference of around 4.67 meV per f.u. We are therefore confident that our results are not affected by the inclusion of relativistic effects.

### 3.3 Energetic stability of the low-pressure *Pnma* and $R\bar{3}m$ phases of $Sb_2Se_3$ at finite temperature

The calculations in the previous section were performed at 0 K without taking into consideration the contributions to the free energy from crystal vibrations (phonons). In order to probe whether these effects could alter the energy ordering between the *Pnma* and $R\bar{3}m$ phases of $Sb_2Se_3$, we performed lattice-dynamics calculations on the equilibrium and compressed structures to evaluate the constant-volume Helmholtz and constant-pressure Gibbs free energies at zero pressure ($F$/$G$; Fig. 3).

$F$ is obtained by summing the lattice energy (here the DFT total energy) and the vibrational contributions to the internal energy and entropy from the zero-point atomic motion and thermal population of the harmonic phonon energy levels.[70] As shown in Fig. 3, $F$ predicts that at zero pressure the $R\bar{3}m$ phase remains the most stable across the temperature range examined with no crossing of the free energy to suggest a transition to the *Pnma* phase. At 0 K, the difference in $F$ between the two phases is 27.24 meV per f.u., which is ~4.53 meV higher than the difference in $H$ due to the addition of the zero-point energy (*i.e.* the differences in the phonon frequencies selectively stabilise the $R\bar{3}m$ phase). At 300 K, the difference between the phases shows a negligible increase from 0.11 meV per F.U. to 27.35 meV.

Another factor that can influence the ordering of two competing phases is thermal expansion. A variation of the lattice volume due to thermal expansion/contraction impacts both the lattice energy and the phonon contributions to the free energy. This can be accounted for through the quasi-harmonic approximation (QHA) where the thermal expansion of the lattice is predicted from the volume dependence of the lattice energy, phonon frequency spectrum and phonon free energy.[70,71] The free energy $F$ is computed for a series of unit-cell volumes and the equilibrium volume and Gibbs free energy $G$ at a finite temperature $T$ are obtained by minimizing $F$ for a given (constant) pressure. Fig. 3 shows the difference in $G$ between the *Pnma* and $R\bar{3}m$ phases of $Sb_2Se_3$. When taking into account the thermal expansion, the $R\bar{3}m$ phase still remains stable phase with respect to the *Pnma* phase from 0–1000 K with a similar energy difference of 29.43 meV at 0 K to

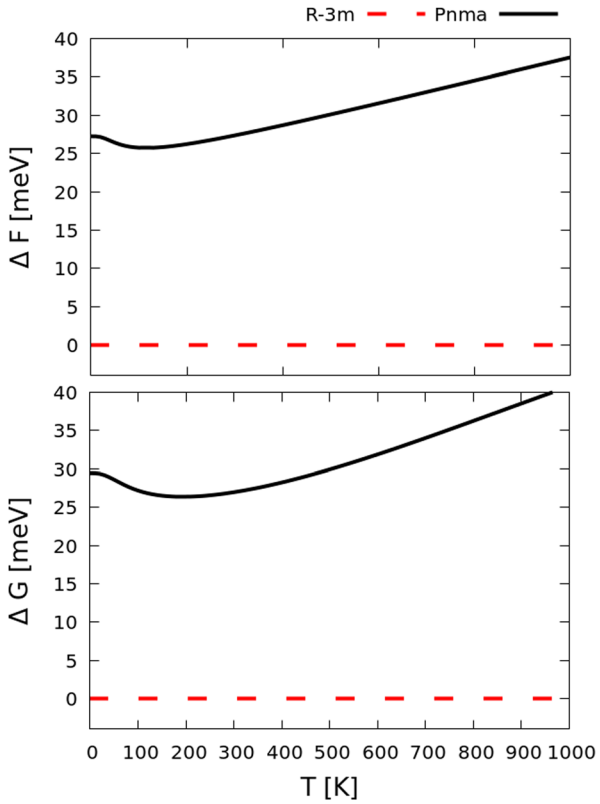


Fig. 3 Constant-volume Helmholtz (top) and Gibbs (bottom) free energies of the *Pnma* phase of $Sb_2Se_3$ (black, solid line) relative to the $R\bar{3}m$ phase (red, dashed line) as a function of temperature at zero applied pressure.

that predicted using the constant-volume $F$, and a slightly smaller difference of 26.96 meV at 300 K.

To investigate the effect of pressure on the free energy, we also computed the difference in the Gibbs energy between the two phases at applied pressures from 0–5 GPa (Fig. 4). For $p$ = 3 and 4 GPa, these calculations predict the $R\bar{3}m$ phase to be the most energetically stable phase across the 0–1000 K temperature range examined, but it can be clearly seen that pressure reduces the energy differences between the two phases. At 4 GPa, the smallest energy difference between the two phases of ~3.25 meV is predicted to occur between 650 and 700 K. Increasing the pressure slightly to 4.2 GPa results in the energies of the two phases becoming nearly equal at around 400 K, and at 4.3 GPa a phase transition from $R\bar{3}m$ to *Pnma* is predicted to occur around this temperature. At 4.5 GPa, the predicted transition temperature decreases to ~200 K, and at 5 GPa, the *Pnma* phase becomes the most energetically favorable structure across the entire temperature range examined.

In summary, free-energy calculations including phonon contributions and thermal expansion at zero applied pressure also predict that the $R\bar{3}m$ phase of $Sb_2Se_3$ is more stable than the *Pnma* phase. Interestingly, at most temperatures both $F$ and $G$ predict an increase in the energy difference, from which we infer that phonon contributions to the free energy selectively stabilise the $R\bar{3}m$ phase, at least at zero applied pressure. At low

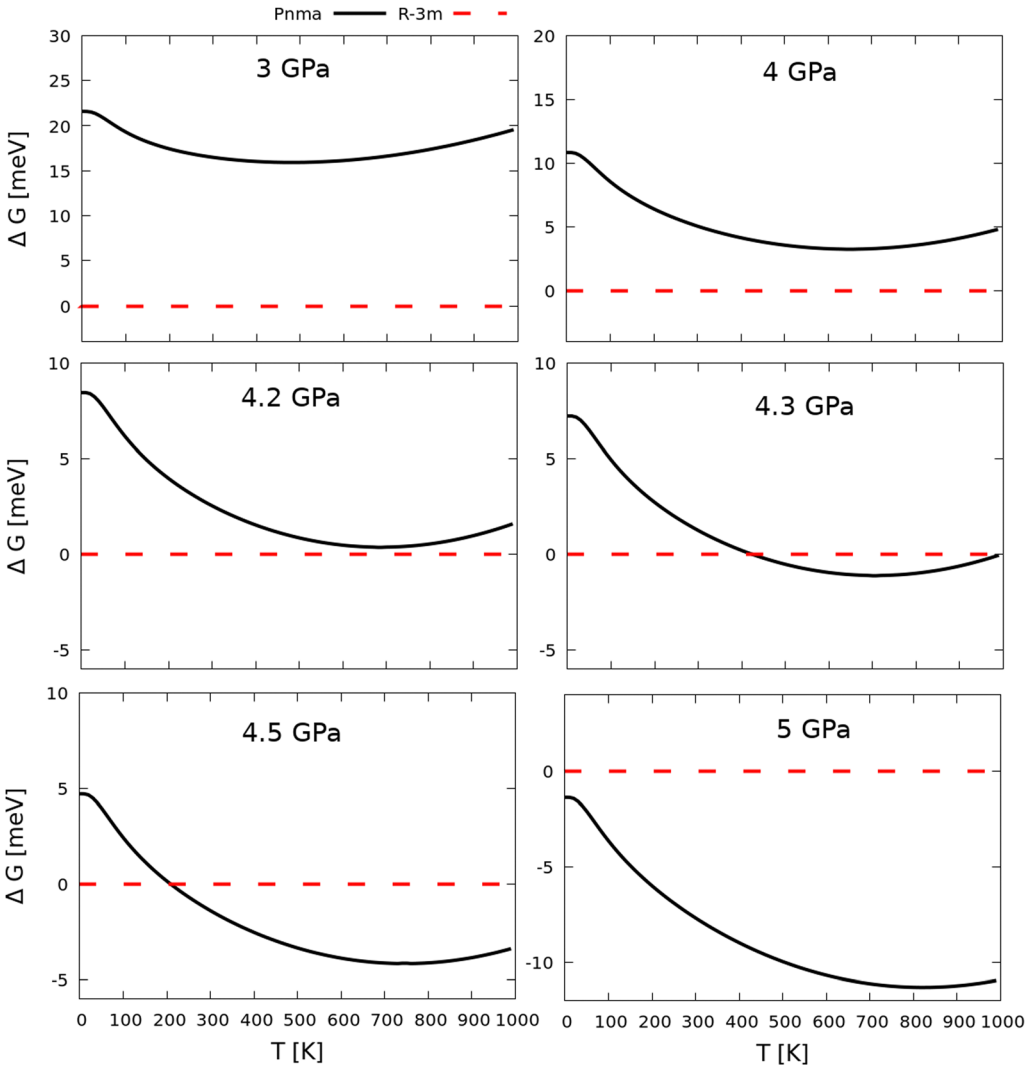


Fig. 4 Gibbs free energies of the *Pnma* phase of $Sb_2Se_3$ (black, solid line) relative to the $R\bar{3}m$ phase (red, dashed line) as a function of temperature at applied pressures from 3–5 GPa.

finite pressures between 4.2 and 4.4 GPa, the Gibbs free energies predict a pressure-induced transition between the $R\bar{3}m$ and *Pnma* phases near room temperature, and predict the *Pnma* phase to be stable above 5 GPa, which is similar to the 4.8 GPa transition pressure predicted from the 0 K enthalpies without zero-point energy corrections (*c.f.* Fig. 2). The small decrease in the predicted transition pressure can be attributed to the different impacts of volume changes on the phonon spectra of the two phases.

### 3.4 Dynamical stability of the *Pnma* and $R\bar{3}m$ phases of $Sb_2Se_3$

Energetic stability is a necessary but not sufficient condition for a structural phase to be synthetically accessible. A second criterion is that one should also confirm the dynamical stability of the system, which can be performed by studying the phonon frequency spectrum. If imaginary frequencies are present in the phonon dispersion, this is an indication that the system is not a minimum on the structural potential-energy surface (and is instead *e.g.* a transition state or a hilltop in multidimensional space), and would spontaneously convert to a lower-energy structure and thus be kinetically unstable under a given set of conditions.[72–77]

We therefore investigated the dynamical stability of the $R\bar{3}m$ phase of $Sb_2Se_3$ to confirm whether this structure could potentially be synthesized under or close to ambient conditions. To do so, we evaluated the phonon band dispersion and density of states (DoS) curves of the $R\bar{3}m$ phase at zero pressure and different temperatures using the QHA method described in the previous section (Fig. 5). For comparison, we also present the phonon band structure and DoS of the *Pnma* phase. Both structures show real frequencies across the whole of the Brillouin zone, indicating that both are dynamically stable under ambient conditions (*i.e.* 0 GPa and room temperature) and confirming that, as implied by the energetics calculations, both phases should be accessible under appropriate synthesis conditions.

 

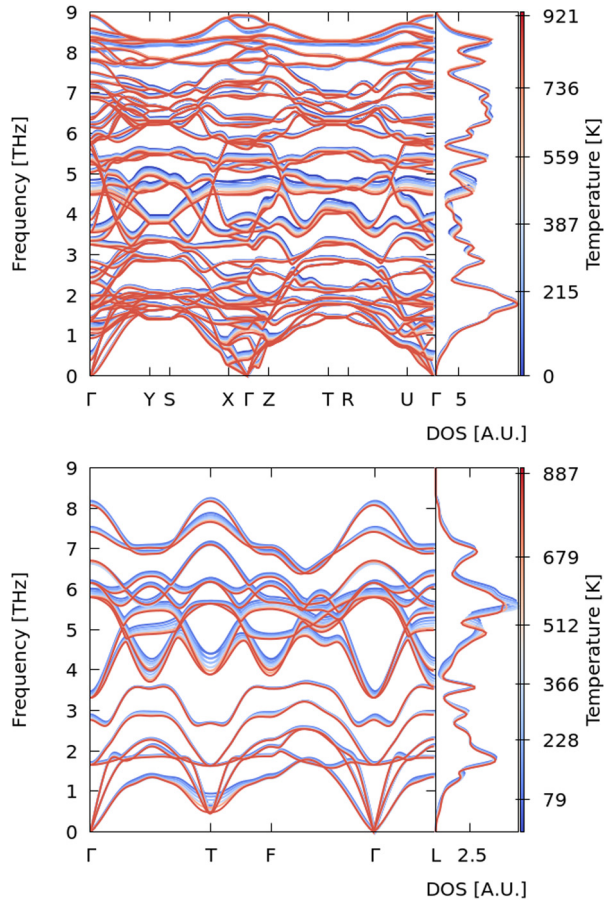


Fig. 5 Quasi-harmonic phonon dispersion curves for *Pnma* (top) and $R\bar{3}m$ $Sb_2Se_3$ (bottom). The color gradient runs from blue (low *T*) to red (high *T*) for temperatures between ~0 and 1000 K.

In this context, we note that these results are consistent with a recent theoretical study of the $R\bar{3}m$ phase of $Sb_2Se_3$, which reported phonon dispersion curves and confirmed the dynamical stability of this phase at 0 GPa and 0 K.[23] This study also reported formation energies as evidence for the stability of the $R\bar{3}m$ phase. In addition, *ab initio* molecular dynamics calculations also confirmed that the $R\bar{3}m$ phase remains structurally stable at 300 K.[23]

### 3.5 Mechanical stability of the *Pnma* and $R\bar{3}m$ phases of $Sb_2Se_3$

Having established the energetic and dynamical stabilities of the phase $R\bar{3}m$ of $Sb_2Se_3$ at zero pressure, we also checked the mechanical (elastic) stability as a third condition that must be fulfilled for this system to be synthetically accessible. This is achieved by calculating the elastic constants and confirming that they obey the Born stability criteria when the solid is subjected to homogeneous deformations.[72,78,79] Table 2 lists the calculated elastic constants of the *Pnma* and $R\bar{3}m$ phases of $Sb_2Se_3$ at zero pressure.

We also computed the linear compressibility of both phases using ELATE analysis tools.[48] For both phases, only directions corresponding to positive linear compressibilities were obtained, indicating that both phases are mechanically stable under ambient conditions. In the case of the $R\bar{3}m$ phase, we obtained linear compressibilities between $\beta_{min}$ = 4.9 $TPa^{-1}$ (hexagonal *a*-axis) and $\beta_{max}$ = 19.5 $TPa^{-1}$ (hexagonal *c*-axis) with an anisotropy value of 3.95. For the *Pnma* phase, the compressibilities fall between $\beta_{min}$ = 3.7 $TPa^{-1}$ (*b*-axis) and $\beta_{max}$ = 25.7 $TPa^{-1}$ (*a*-axis) with an anisotropy of 6.87. These values are of the same order as the experimental axial compressibilities of the *Pnma* phase of $Sb_2Se_3$ ($\beta_a$ = 15.2 $TPa^{-1}$, $\beta_b$ = 3.9 $TPa^{-1}$, and $\beta_c$ = 8.3 $TPa^{-1}$).[62] Table 3 summarises the elastic moduli calculated from the elastic constants, and we note that the bulk modulus of the *Pnma* phase of $Sb_2Se_3$ (31.8 GPa) is similar to that obtained from the Birch–Murnaghan fit (*c.f.* Table 1), which confirms that the elastic constants are adequately converged.

The calculated elastic constants in Table 2 fulfill the necessary and sufficient Born criteria for the mechanical stability of orthorhombic (eqn (1)) and rhombohedral (eqn (2)) systems.[79] The calculated elastic constants therefore indicate that both the $R\bar{3}m$ and *Pnma* phases of $Sb_2Se_3$ are mechanically stable under ambient conditions.

$$c_{11}, c_{44}, c_{55}, c_{66} > 0;\ c_{11}c_{22} > c_{12}^2;\ c_{11}c_{22}c_{33} + 2c_{12}c_{13}c_{23} - c_{11}c_{23}^2 - c_{22}c_{13}^2 - c_{33}c_{12}^2 > 0 \quad (1)$$

$$c_{11} > |c_{12}|;\ c_{44} > 0;\ c_{13}^2 < \frac{1}{2}c_{33}(c_{11} + c_{12});\ c_{14}^2 < \frac{1}{2}c_{44}(c_{11} - c_{12}) = c_{44}c_{66} \quad (2)$$

The elastic tensors of the *Pnma* phase of $Sb_2Se_3$ have previously been calculated.[49] However, in these calculations,

Table 3 Calculated elastic properties of the *Pnma* and $R\bar{3}m$ phases of $Sb_2Se_3$ at zero pressure obtained within the Voigt approximation using the ELATE analysis tool: bulk modulus, $B_0$, Young's modulus, *E*, shear modulus, *G* and Poisson's ratio, $\upsilon$

| | $B_0$ (GPa) | *E* (GPa) | *G* (GPa) | $\upsilon$ |
|---|---|---|---|---|
| *Pnma* | 31.82 | 44.10 | 17.38 | 0.27 |
| $R\bar{3}m$ | 40.00 | 65.56 | 26.72 | 0.23 |

Table 2 Calculated elastic constants $c_{ij}$ (GPa) of the *Pnma* and $R\bar{3}m$ phases of $Sb_2Se_3$ at zero pressure

| | $c_{11}$ | $c_{22}$ | $c_{33}$ | $c_{12}$ | $c_{13}$ | $c_{23}$ | $c_{44}$ | $c_{55}$ | $c_{66}$ |
|---|---|---|---|---|---|---|---|---|---|
| *Pnma* | 30.92 | 81.65 | 55.20 | 17.32 | 15.10 | 26.89 | 17.83 | 25.21 | 7.69 |
| | $c_{11} = c_{22}$ | | $c_{33}$ | $c_{12}$ | $c_{13} = c_{23}$ | $c_{15} = -c_{25} = c_{46}$ | | $c_{44} = c_{55}$ | $c_{66}$ |
| $R\bar{3}m$ | 90.81 | | 40.21 | 25.85 | 21.61 | −12.00 | | 25.10 | 32.48 |

the components were overestimated as clearly shown by the comparison of the bulk modulus with experiments. Part of the disagreement could be due to the low cut-off energy used in these calculations.

In summary, our calculations on $Sb_2Se_3$ demonstrate that the *Pnma* and $R\bar{3}m$ phases are energetically competitive under ambient conditions and that both phases are dynamically and mechanically stable. Given that it should in principle be possible to obtain the $R\bar{3}m$ phase, but it has yet to be reported experimentally, it may be that the $R\bar{3}m$ phase is difficult to form kinetically, *i.e.* that the *Pnma* phase is formed faster than the $R\bar{3}m$ phase under typical synthesis conditions. We note that the $R\bar{3}m$ phase did not appear on the pressure/temperature phase diagram prepared by Pfeiffer *et al.*,[80] although this study did not attempt to vary the synthesis conditions at close to ambient pressure, which the present calculations suggest would allow this phase to be formed. Since our calculations increase the possibility that the $R\bar{3}m$ phase could potentially be prepared under slightly non-equilibrium conditions, to help identify $R\bar{3}m$ $Sb_2Se_3$ in future experiments we provide in the following section a reference structure and vibrational spectra.

### 3.6 Crystal structure and vibrational spectra of $R\bar{3}m$ $Sb_2Se_3$

Table 4 lists the predicted equilibrium crystal structure (lattice parameters and atomic positions) of $R\bar{3}m$ $Sb_2Se_3$ obtained using the PBEsol XC functional. (The calculations with PBE + D2 and LDA yield slightly different lattice parameters, *viz.* PBE + D2 – $a_0$ = 4.02 Å, $c_0$ = 28.81 Å and $V_0$ = 403.89 Å$^3$; and LDA – $a_0$ = 3.99 Å, $c_0$ = 27.58 Å, and $V_0$ = 381.61 Å$^3$.) The predicted lattice parameters are in good agreement with those reported for other tetradymite-like sesquichalcogenides.[81] The optimised $a_0$ and $c_0$ are slightly smaller than those of $Bi_2Se_3$ and much smaller than those of $Sb_2Te_3$.[81]

We have also computed the Raman and infrared (IR) spectra of the equilibrium structure to provide spectral signatures that could be used to identify the $R\bar{3}m$ phase in experiments using routine characterisation techniques (Fig. 6).

The frequencies, irreducible representations and IR/Raman intensities associated with each of the zone-centre (Γ-point) vibrational modes are listed in Table 5.

The inversion symmetry in the $R\bar{3}m$ structure leads to a mutual exclusion between the IR and Raman activities of the modes, with each spectrum being characterized by four bands.[81] The most intense Raman band occurs at around 139 cm$^{-1}$ ($E_g$), while a second prominent feature is predicted at ~204 cm$^{-1}$ ($A_{1g}$). The frequency of this $A_{1g}$ mode is higher than that in $Bi_2Se_3$ but lower than that in $In_2Se_3$, as expected from the difference in mass between In, Sb and Bi.[82,83] Lower-frequency $E_g$ and $A_{1g}$ modes with much lower intensities are also found around 53 and 84 cm$^{-1}$, respectively, which are again slightly blue-shifted when compared to the corresponding frequencies calculated for $Bi_2Se_3$.[82] There are four IR-active modes, two with $E_{1u}$ symmetry (87 and 132 cm$^{-1}$) and two with $A_{2u}$ symmetry (145 and 183 cm$^{-1}$). Of these, the 87 cm$^{-1}$ mode is the most prominent in the spectrum, while

Table 4 Predicted equilibrium lattice parameters and atomic positions for the hexagonal unit cell of the $R\bar{3}m$ phase of $Sb_2Se_3$

| | $c_0$ (Å) | $V_0$ (Å3) | $B_0$ (GPa) | $B_0'$ |
|---|---|---|---|---|
| 4.01 | 28.16 | 392.16 | 50.56 | 4.16 |

| | Site | Sym. | x | y | Z |
|---|---|---|---|---|---|
| $Sb_1$ | 6c | 3m | 0.00000 | 0.00000 | 0.60082 |
| $Se_1$ | 3a | −3m | 0.00000 | 0.00000 | 0.00000 |
| $Se_2$ | 6c | 3m | 0.00000 | 0.00000 | 0.78792 |

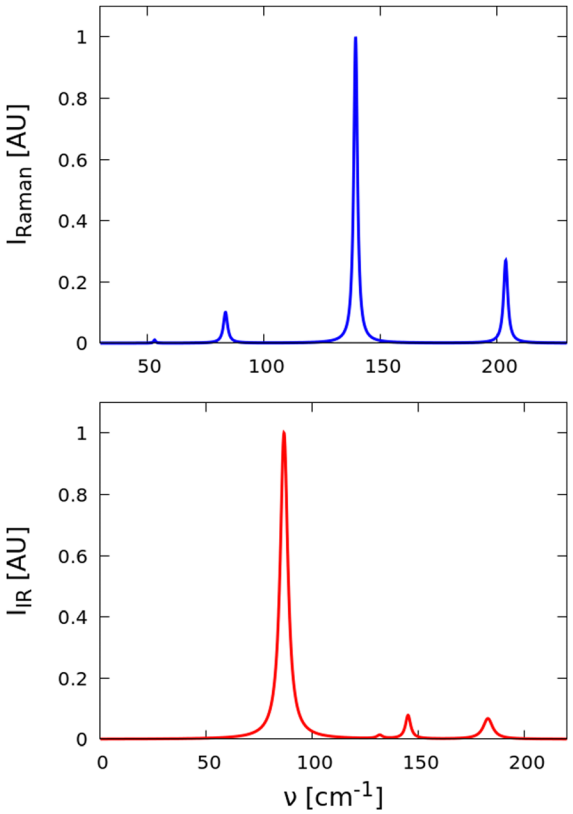


Fig. 6 Simulated Raman (top) and infrared (IR; bottom) spectra of equilibrium $R\bar{3}m$ $Sb_2Se_3$. Spectral lines have been broadened with the calculated intrinsic mode linewidths at 300 K.

Table 5 Calculated vibrational modes of the $R\bar{3}m$ phase of the equilibrium structure of $Sb_2Se_3$. The three acoustic modes span an irreducible representations of $\Gamma_{acoustic} = A_{2u} + E_u$, and the remaining 12 optic modes span a representation of $\Gamma_{optic} = 2E_g$ (Raman) + $2A_{1g}$ (Raman) + $2E_u$ (IR) + $2A_{2u}$ (IR)

| | Frequency (cm$^{-1}$) | Raman intensity (10$^5$ Å$^4$ amu$^{-1}$) | IR intensity (e$^2$ amu$^{-1}$) | Spectral linewidth (cm$^{-1}$) |
|---|---|---|---|---|
| $E_g$ | 53.3 | 0.02 | Inactive | 1.02 |
| $A_{1g}$ | 83.7 | 0.37 | Inactive | 2.11 |
| $E_u$ | 86.6 | Inactive | 3.47 | 4.32 |
| $E_u$ | 131.7 | Inactive | 0.03 | 3.13 |
| $E_g$ | 139.4 | 3.32 | Inactive | 1.89 |
| $A_{2u}$ | 145.1 | Inactive | 0.18 | 2.94 |
| $A_{2u}$ | 182.8 | Inactive | 0.29 | 5.38 |
| $A_{1g}$ | 203.8 | 1.02 | Inactive | 2.16 |

the second $E_u$ mode at 132 $cm^{-1}$ is comparatively weak. The two $A_{2u}$ bands have moderate and comparable intensities and form a pair of smaller features at higher frequencies. As expected, given the mass difference, the IR-active modes in $Sb_2Se_3$ again have slightly higher frequencies than those calculated for $Bi_2Se_3$.[82]

It is also worth comparing our predicted structural and vibrational properties of $R\bar{3}m$ $Sb_2Se_3$ to the published works pertaining to the possible synthesis of this phase. In 2013, Bera *et al.*[25] claimed to have observed the $R\bar{3}m$ phase of $Sb_2Se_3$ at room temperature. However, the experimental lattice parameters were not disclosed and the reported Raman spectrum is not consistent with our theoretical spectrum, although our spectrum is consistent with simulations performed in the same study. We also note that our calculations of the pressure coefficients for the Raman- and IR-active modes of tetradymite $Sb_2Se_3$ (not shown) indicate that all the modes should show positive pressure coefficients, which is again consistent with the theoretical results shown in ref. 25.

If we consider that the band gap of tetradymite-like $Sb_2Se_3$ is similar to or even larger than that of tetradymite-like $Bi_2Se_3$, we would expect the Raman spectrum of tetradymite-like $Sb_2Se_3$ to be similar. We may therefore conclude that the experimental Raman spectra reported in ref. 25 are not consistent with tetradymite-like $Sb_2Se_3$. In this vein, we note that the appearance of soft Raman modes with a negative pressure coefficient at low pressures as reported in ref. 25 is similar to those of Se and Te nano- or micro-clusters.[84–87] Such features are either formed during synthesis or induced by laser heating in Raman scattering measurements at high laser powers, as has recently been discussed.[87]

Recently, Matetskiy *et al.*[32] claimed to have observed the tetradymite-like phase of $Sb_2Se_3$ in MBE-deposited layers over a thick buffer layer of tetradymite-like $Bi_2Se_3$. This study reported a lattice parameter of $a_0$ = 4.048 Å for quintuple layers of tetradymite-like $Sb_2Se_3$. The quintuple layers were observed by scanning-tunnelling microscopy (STM) to be of ~1 nm in thickness, meaning that the $c_0$ lattice parameter, corresponding to three quintuple layers, would be ~30 Å. Both the reported $a_0$ and $c_0$ lattice parameters are consistent with our calculated values. Furthermore, the electron dispersion obtained from angle-resolved photoemission spectroscopy (ARPES) is compatible with the $R\bar{3}m$ phase. It is therefore highly probable that tetradymite-like $Sb_2Se_3$ was synthesized for the first time in this study. Unfortunately, this study did not report vibrational spectra that would allow for additional comparison to our predictions.

### 3.7 On the observation of the $R\bar{3}m$ phase of $A_2X_3$ sesquichalcogenides

An analysis of bonding in layered materials under ambient conditions, including tetradymite-like $B_2^VX_3^{VI}$ and $A^{VI}B_2^VX_4^{VI}$ chalcogenides and also transition metal dichalcogenides (TMDs), has recently been performed by plotting the van der Waals (vdW) gap spacing *vs.* the X–X plane spacing.[88] The vdW gap spacing is defined as the interplanar distance across the interlayer space, whereas the X–X plane distance is the interplanar width across the intralayer space.[88,89] In ref. 88, it was concluded from the strong correlation that TMDs show a pure interlayer vdW interaction, whereas the tetradymite-like chalcogenides do not because the vdW gap spacing is much smaller than expected for their X–X plane spacing, which is indicative of a stronger interlayer interaction than that expected for pure vdW interactions.

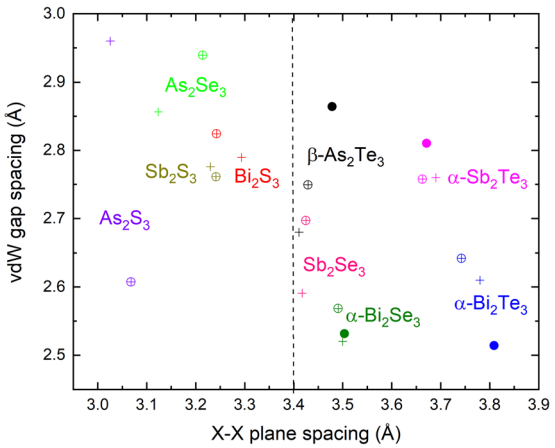


Fig. 7 Size of van der Waals gap *vs.* chalcogenide X–X plane spacing in the $R\bar{3}m$ phases of $A_2X_3$ sesquichalcogenides (A = As, Sb, Bi and X = Te, Se, S). The data obtained from our theoretical calculations using dispersion-corrected PBE are shown as circles with crosses. For comparison, we also show theoretical PBEsol calculations on α-$Bi_2Se_3$, α-$Bi_2Te_3$ and α-$Sb_2Te_3$ from ref. 89 (crosses) and experimental measurements on β-$As_2Te_3$, α-$Bi_2Se_3$, α-$Bi_2Te_3$ and α-$Sb_2Te_3$ from ref. 93–96 (dots).

It has recently been suggested that the vdW gap spacings in tetradymite-like group-15 sesquichalcogenides are smaller than those found for pure vdW materials, *e.g.* GaSe, InSe and TMDs. This has been attributed to the presence of the extra delocalized electrons between the layers that contribute an electrostatic component to the bonding that is not present in pure vdW materials.[24,90] These delocalized electrons arise from a new type of bonding, termed "metavalent bonding", between the cations and anions inside the quintuple layers of the tetradymite-like structure, which has been demonstrated by the observation of a net charge difference between the layers in group-15 sesquichalcogenides[91] and through a topological study of the electronic charge density of $SnSb_2Te_4$.[92] In essence, the metavalent bonding results in the cations and anions providing extra electrons to the space between the layers, which in turn supports a stronger interlayer interaction.

In Fig. 7, we compare experimental (where available) and theoretical vdW gap spacings against X–X plane spacings for the full set of tetradymite-like $B_2^VX_3^{VI}$ (B = As, Sb, Bi; X = S, Se, Te) sesquichalcogenides.[88,89] (The theoretical results are obtained with PBEsol and dispersion-corrected PBE.)

Fig. 7 shows that the compounds usually synthesized in the tetradymite-like structure, *viz.* β-$As_2Te_3$, α-$Sb_2Te_3$, α-$Bi_2Te_3$ and α-$Bi_2Se_3$, have a very small vdW gap spacings (typically below 2.9 Å) and large X–X plane spacings (typically above 3.4 Å). It is particularly striking that the Te–Te plane spacing in β-$As_2Te_3$ is

below 3.5 Å, which is very different to other Te sesquichalcogenides and close to the Se–Se plane spacings in Se sesquichalcogenides such as $Bi_2Se_3$. From this analysis, we can therefore inferr that all the compounds with a stable tetradymite-like structure under ambient conditions (see Fig. 5 of ref. 88) have relatively small vdW gap spacings and X–X plane spacings between 3.4 and 3.8 Å. Since $As_2Se_3$ and $Sb_2Se_3$ do not usually crystallize in the tetradymite-like structure, it can similarly be inferred that X–X plane spacings below 3.4 Å and vdW gap spacings above 2.9 Å are outside the limit of stability for tetradymite structures of the $B_2^VX_3^{VI}$ and $A^{VI}B_2^VX_4^{VI}$ chalcogenides. This is consistent with: (i) the locations of α-$Bi_2Se_3$ and β-$As_2Te_3$ close to the lower limit of the X–X plane spacing; (ii) the metastable tetradymite-like phase of β-$As_2Te_3$ being obtained under ambient conditions; and (iii) the metastable orthorhombic *Pnma* phase of $Bi_2Se_3$ (guanajuatite) being obtained under ambient conditions.[17,97–99] The latter is isostructural to $Bi_2S_3$, $Sb_2S_3$ and $Sb_2Se_3$ and has been observed in high-pressure studies on α-$Bi_2Se_3$ (paraguanajuatite) on decreasing the pressure.[54,69]

Most importantly, the vdW gap spacings and X–X plane spacings calculated for $Sb_2Se_3$ with PBEsol and dispersion-corrected PBE are similar to those obtained for other group-15 tetradymite-like sesquichalcogenides. This lends further support to the idea that the $R\bar{3}m$ phase of $Sb_2Se_3$ should be synthetically accessible with a structure similar to that predicted in our calculations. Unfortunately, despite the fact that $R\bar{3}m$ $Sb_2Se_3$ does appear to have been synthesized recently,[32,88] a complete structural characterization has yet to be reported and therefore several of our calculated parameters cannot be compared to experimental measurements. We thus hope that the present study will stimulate further attempts to prepare and characterise the $R\bar{3}m$ phase of $Sb_2Se_3$.

Finally, the analysis in Fig. 7 shows that all the group-15 sesquisulphides for which the theoretical $R\bar{3}m$ structures have X–X plane spacings below 3.4 Å do not seem to be stable in this phase under ambient conditions according to our calculations. This is in good agreement with the high predicted enthalpies of these phases of $Sb_2S_3$ and $Bi_2S_3$. However, this does not necessarily mean that the $R\bar{3}m$ phase of these compounds cannot be synthesized, as $R\bar{3}m$ $As_2Se_3$ can be prepared at high pressure and high temperature, which indicates that the tetradymite-like structure of $As_2Se_3$ is metastable under ambient conditions.[80,100–102] It is therefore possible that tetradymite-like $As_2S_3$, $Sb_2S_3$ and $Bi_2S_3$ could also potentially be synthesized under the right conditions.

# 4 Conclusions

We have performed a comparative theoretical study of the *Pnma* and $R\bar{3}m$ phases of $Sb_2S_3$, $Bi_2S_3$, and $Sb_2Se_3$ at applied pressures of up to 10 GPa. Our calculations predict that at ambient pressure the $R\bar{3}m$ (tetradymite-like) phase of $Sb_2Se_3$ is energetically more stable than the *Pnma* phase, in contrast to $Sb_2S_3$ and $Bi_2S_3$. This result contradicts the fact that all three compounds are usually grown on the *Pnma* phase. Further energetic studies of both $Sb_2Se_3$ phases show that the higher energetic stability of the $R\bar{3}m$ phase with respect to the *Pnma* phase is predicted by three different XC functionals and is unaffected by the phonon contributions to the free energy and thermal expansion at finite temperature. Lattice dynamics and elastic tensor calculations further show that both the phases of $Sb_2Se_3$ are dynamically and mechanically stable at zero pressure. Our calculations therefore suggest that the formation of this phase should be feasible under close to ambient conditions.

To aid in its identification, we have provided a theoretical crystal structure and predicted IR and Raman spectra. We have also discussed our results against the only two published works, to the best of our knowledge, that have claimed to have synthesized tetradymite-like $Sb_2Se_3$, and concluded that there is a high probability that this phase has recently been synthesized by molecular beam epitaxy on a thick buffer layer of tetradymite-like $Bi_2Se_3$.

Finally, we have discussed the stability of the $R\bar{3}m$ structure for all group-15 sesquichalcogenides by comparing the vdW gap and X–X plane spacings, which again suggests that the $R\bar{3}m$ phase of $Sb_2Se_3$ should be synthetically accessible. We hope that this work will stimulate further investigation of tetradymite-like $Sb_2Se_3$ and the corresponding phases of $As_2Se_3$ and other sesquichalcogenides. These sesquichalcogenide phases could potentially show topological properties interesting for spintronics and quantum computation at moderate pressures, and also be of interest as phase change materials and highly-efficient thermoelectric materials, and for photonic devices.

# 5 Appendices

## 5.1 Enthalpy *vs.* pressure curves obtained using different exchange–correlation functionals

In order to verify that the variation of the enthalpy differences between the *Pnma* and $R\bar{3}m$ phases of the three sesquichalcogenides with pressure presented in Fig. 2 was not due to an issue with the PBEsol functional, we performed similar calculations using dispersion-corrected PBE (PBE-D2; Fig. 8) and the LDA (Fig. 9). For $Sb_2Se_3$ both functionals also predict the $R\bar{3}m$ phase to be the most energetically stable under ambient conditions. There is however some variation in the predicted transition pressure, with PBEsol and the LDA (Fig. 9) predicting similar pressures but PBE-D2 predicting a slightly higher transition point (Fig. 8).

## 5.2 Electronic properties of the $R\bar{3}m$ structural phase of $Sb_2Se_3$

Fig. 10 shows the electronic band structure and atom- and orbital-projected (partial) density of states of the $R\bar{3}m$ phase of $Sb_2Se_3$. We have considered spin–orbit coupling effects in this calculation due to their importance in determining the electronic properties of many potential topological insulators. The

 

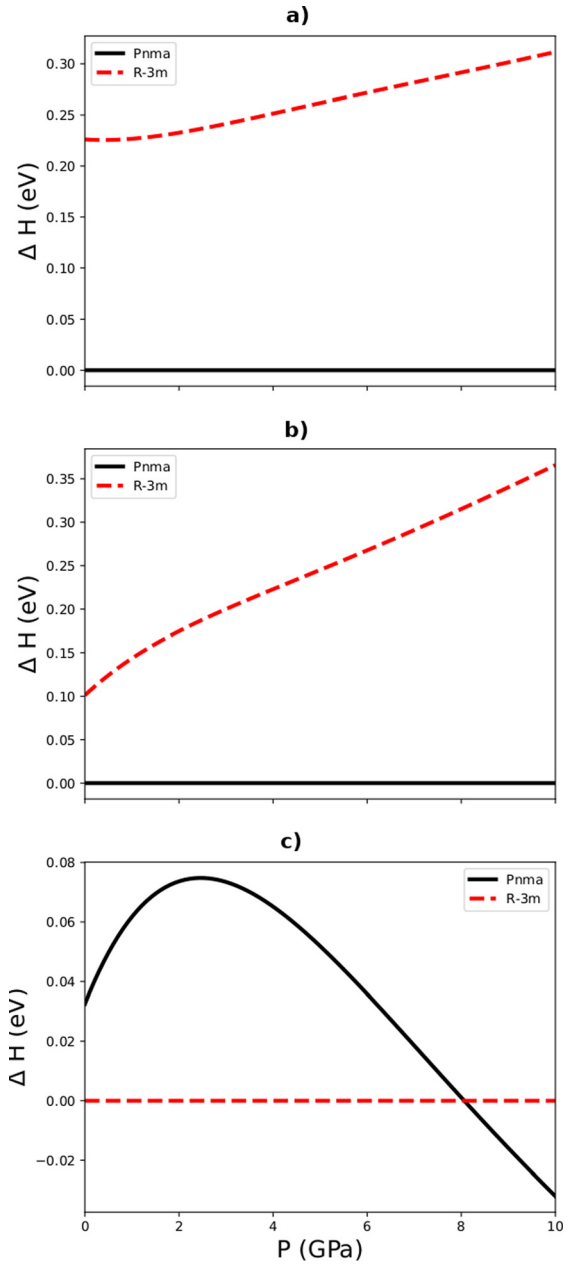


Fig. 8 Calculated relative enthalpy *vs.* pressure up to 10 GPa for the *Pnma* and $R\bar{3}m$ phases of $Sb_2S_3$ (a), $Bi_2S_3$ (b) and $Sb_2Se_3$ (c) relative to the lowest-energy phases at ambient pressure, *viz.* the *Pnma* phases of $Sb_2S_3$ and $Bi_2S_3$ and the $R\bar{3}m$ phase of $Sb_2Se_3$, obtained using PBE-D2.

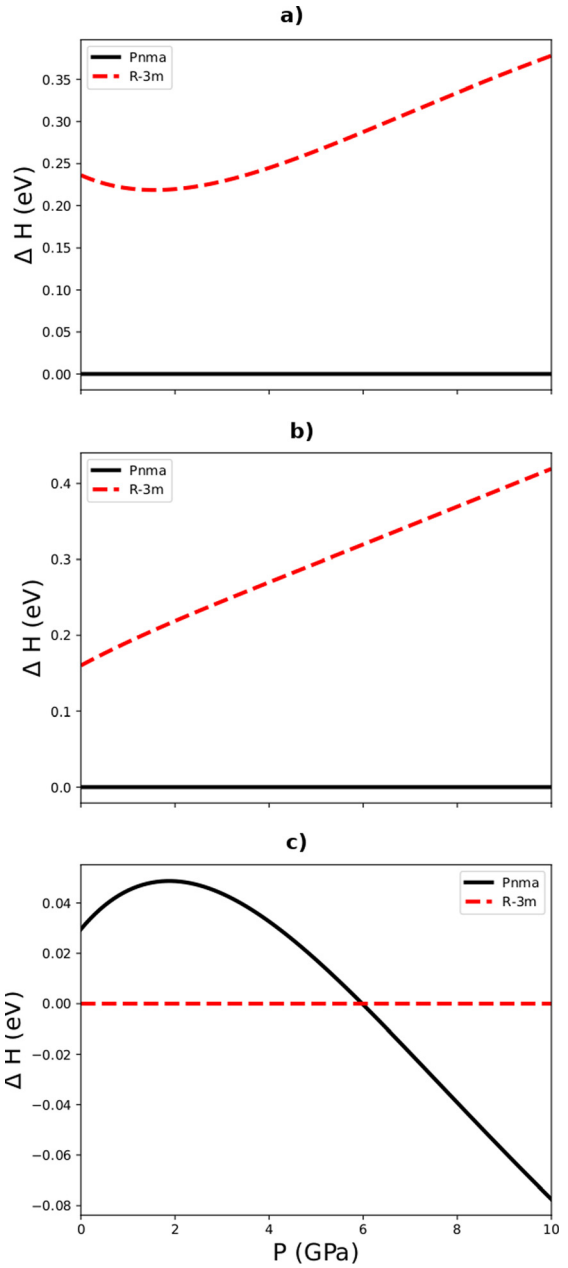


Fig. 9 Calculated enthalpy *vs.* pressure up to 10 GPa for the *Pnma* and $R\bar{3}m$ phases of $Sb_2S_3$ (a), $Bi_2S_3$ (b) and $Sb_2Se_3$ (c) relative to the lowest-energy phase at ambient pressure, *viz.* the *Pnma* phases of $Sb_2S_3$ and $Bi_2S_3$ and the $R\bar{3}m$ phase of $Sb_2Se_3$, obtained using the LDA.

valence band maximum (VBM) is mostly composed of Se p states, whereas the conduction band minimum (CBM) is a hybridization of Se and Sb p states with a small contribution from Se s states. The band gap is direct and located along the $\Gamma$–$Z$ segment of the dispersion in the vicinity of the $\Gamma$ point. Both the VBM and CBM show a "Mexican-hat" feature - indentation of the band dispersion - which indicates that our DFT+SoC calculations predict the $R\bar{3}m$ phase of $Sb_2Se_3$ to be a topological insulator at ambient pressure. $Sb_2Se_3$ differs from similar topological insulators such as $Bi_2Te_3$[104] and $Bi_2Se_3$[105] for which at zero pressure this feature only occurs in the VBM but at moderate pressures the CBM also starts to develop a "Mexican-hat" feature. The calculated PBEsol band gap is around 0.23 eV. From a parabolic fitting of the band edges,[103] we obtain a hole effective mass $m_h = -0.107$ and an electron effective mass $m_e = 0.098$.

## Author contributions

E. L. d. S., M. C. S., J. M. S., P. R. H. and A. M. performed the *ab initio* calculations. E. L. d. S., M. C. S., J. M. S., P. R. H.,

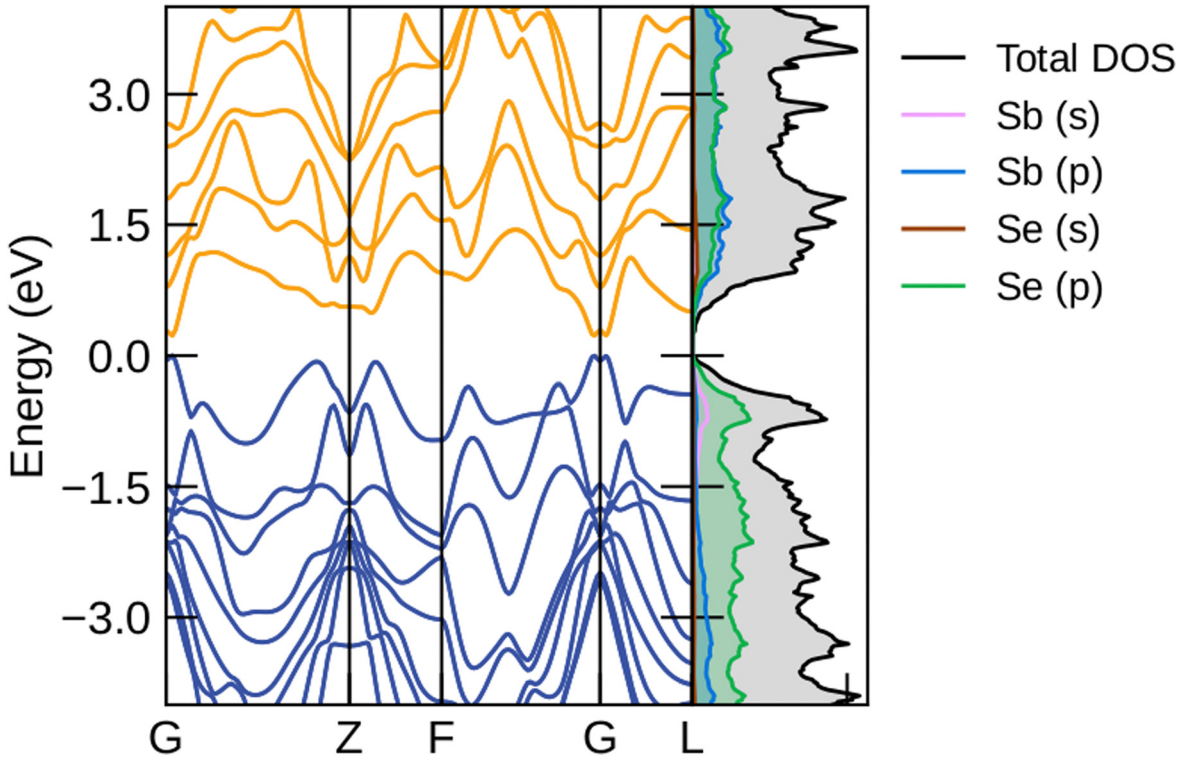


Fig. 10 Electronic band structure (left panel) and partial density of states (right panel) of the $R\bar{3}m$ phase of $Sb_2Se_3$ obtained using PBEsol and including spin–orbit coupling (SoC) effects. The figure was plotted using the Python toolkit SUMO.[103]

A. M., D. M. G., R. V., and F. J. M. contributed to the interpretation and discussion of results. F. J. M. supervised the project. E. L. d. S., M. C. S., J. M. S., P. R. H., A. M., D. M. G., R. V., and F. J. M. contributed equally to the discussion and drafting of the paper. All authors have read and agreed to the published version of the manuscript.

## Data availability

Raw data from this study can be obtained from the corresponding author on reasonable request.

## License statement

For the purpose of open access, the author has applied a Creative Commons Attribution (CC BY) licence to any Author Accepted Manuscript version arising.

## Conflicts of interest

There are no conflicts to declare.

## Acknowledgements

This publication is part of the MALTA Consolider Team network (RED2018-102612-T) (MINECO/AEI/10.13039/501100003329), and is supported by I + D + i project PID2019-106383GB41/42/43 (MCIN/AEI/10.13039/501100011033), by the PROMETEO/2018/123(EFIMAT) and CIPROM/2021/075 (GREENMAT) projects (Generalitat Valenciana), and by the European Union Horizon 2020 research and innovation programme under a Marie Sklodowska-Curie grant agreement (785789-COMEX). E. L. d. S., A. M., and P. R.-H. acknowledge computing time provided on the MALTA-Cluster at the University of Oviedo and on the MareNostrum facility through Red Española de Supercomputación (RES) with technical support provided by the Barcelona Supercomputing Center (QCM-2018-3-0032). E. L. d. S. also acknowledges the Network of Extreme Conditions Laboratories (NECL), financed by FCT and co-financed by NORTE 2020 through the Portugal 2020 and FEDER programmes. J. M. S. is grateful to UK Research and Innovation for the support of a Future Leaders Fellowship (MR/T043121/1) and to the University of Manchester for the previous support of a Presidential Fellowship.

## References

1 Y. L. Chen, J. G. Analytis, J.-H. Chu, Z. K. Liu, S.-K. Mo, X. L. Qi, H. J. Zhang, D. H. Lu, X. Dai, Z. Fang, S. C. Zhang, I. R. Fisher, Z. Hussain and Z.-X. Shen, *Science*, 2009, **325**, 178.
2 H. Zhang, C.-X. Liu, X.-L. Qi, X. Dai, Z. Fang and S.-C. Zhang, *Nat. Phys.*, 2009, **5**, 438.
3 M. Z. Hasan and C. L. Kane, *Rev. Mod. Phys.*, 2010, **82**, 3045.
4 J. Black, E. M. Conwell, L. Seigle and C. W. Spencer, *J. Phys. Chem. Solids*, 1957, **2**, 240.

 

5 M. R. Filip, C. E. Patrick and F. Giustino, *Phys. Rev. B: Condens. Matter Mater. Phys.*, 2013, **87**, 205125.
6 S.-J. Sa Moon, Y. Itzhaik, J.-H. Yum, S. M. Zakeeruddin, G. Hodes and M. Gräzel, *J. Phys. Chem. Lett.*, 2010, **1**, 1524.
7 C. E. Patrick and F. Giustino, *Adv. Funct. Mater.*, 2011, **21**, 4663.
8 Y. Zhou, L. Wang, S. Chen, S. Qin, X. Liu, J. Chen, D. Xue, M. Luo, Y. Cao, Y. Cheng, E. Sargent and J. Tang, *Nat. Photonics*, 2015, **9**, 409.
9 L. Wang, D. Li, K. Li, C. Chen, H.-X. Deng, L. Gao, Y. Zhao, F. Jiang, L. Li, F. Huang, Y. He, H. Song, G. Niu and J. Tang, *Nat. Energy*, 2017, **2**, 17046.
10 O. Rabin, J. Perez, J. Grimm, G. Wojtkiewicz and R. Weissleder, *Nat. Mater.*, 2006, **5**, 118.
11 K. Yao, Z. Zhang, X. Liang, Q. Chen, L.-M. Peng and Y. Yu, *J. Phys. Chem. B*, 2006, **110**, 21408.
12 L. Cademartiri, F. Scotognella, P. O'Brien, B. Lotsch, J. Thomson, S. Petrov, N. Kherani and G. Ozin, *Nano Lett.*, 2009, **9**, 1482.
13 Mamta, Y. Singh, K. Maurya and V. Singh, *Sol. Energy Mater. Sol. Cells*, 2021, **230**, 111223.
14 S. Chen, T. Liu, Z. Zheng, M. Ishaq, G. Liang, P. Fan, T. Chen and J. Tang, *J. Energy Chem.*, 2022, **67**, 508.
15 Q. Li, W. Zhang, J. Peng, D. Yu, Z. Liang, W. Zhang, J. Wu, G. Wang, H. Li and S. Huang, Adv. Funct. Mater., n/a, 2112776.
16 X. Ma, W. Chen, L. Tong, S. Liu, W. Dai, S. Ye, Z. Zheng, Y. Wang, Y. Zhou, W. Zhang, W. Fang, X. Chen, M. Liao and W. Gao, *Opt. Laser Technol.*, 2021, **143**, 107286.
17 Y. Kang, Q. Zhang, C. Fan, W. Hu, C. Chen, L. Zhang, F. Yu, Y. Tian and B. Xu, *J. Alloys Compd.*, 2017, **700**, 223.
18 V. Kulbachinskii, S. Buga, N. Serebryanaya, N. Perov, V. Kytin, S. Tarelkin, R. Bagramov, N. Eliseev and V. Blank, *J. Phys.: Conf. Ser.*, 2018, **969**, 012152.
19 M. A. Tumelero, L. C. Benetti, E. Isoppo, R. Faccio, G. Zangari and A. A. Pasa, *J. Phys. Chem.*, 2016, **120**, 11797.
20 N. Serebryanaya, S. Buga, R. Bagramov, I. Pahomov, N. Eliseev and V. Blank, *Phys. Status Solidi B*, 2020, **257**, 2000145.
21 W. Liu, X. Peng, C. Tang, L. Sun, K. Zhang and J. Zhong, *Phys. Rev. B: Condens. Matter Mater. Phys.*, 2011, **84**, 245105.
22 W. Li, X. Wei, J.-X. Zhu, C. Ting and Y. Chen, *Phys. Rev. B: Condens. Matter Mater. Phys.*, 2013, **89**, 035101.
23 G. Cao, H. Liu, J. Liang, L. Cheng, D. Fan and Z. Zhang, *Phys. Rev. B*, 2018, **97**, 075147.
24 B. J. Kooi and M. Wuttig, *Adv. Mater.*, 2020, **32**, 1908302.
25 A. Bera, K. Pal, D. V. S. Muthu, S. Sen, P. Guptasarma, U. V. Waghmare and A. K. Sood, *Phys. Rev. Lett.*, 2013, **110**, 107401.
26 J. Ibañez, J. A. Sans, C. Popescu, J. López-Vidrier, J. J. Elvira-Betanzos, V. P. Cuenca-Gotor, O. Gomis, F. J. Manjón, P. Rodríguez-Hernández and A. Muñoz, *J. Phys. Chem. C*, 2016, **120**, 10547.
27 I. Efthimiopoulos, J. Zhang, M. Kucway, C. Park, R. Ewing and Y. Wang, *Sci. Rep.*, 2013, **3**, 2665.
28 J. Anversa, S. Chakraborty, P. Piquini and R. Ahuja, *Appl. Phys. Lett.*, 2016, **108**, 212601.
29 H. Cheng, J. Zhang, P. Yu, C. Gu, X. Ren, C. Lin, X. Li, Y. Zhao, S. Wang and Y. Li, *J. Phys. Chem.*, 2020, **124**, 3421.
30 P. Kong, F. Sun, L. Xing, J. Zhu, S. Zhang, W. Li, X. Wang, S. Feng, X. Yu, J. Zhu, R. C. Yu, W. Yang, G. Shen, Y. Zhao, R. Ahuja, H. Mao and C. Jin, *Sci. Rep.*, 2014, **4**, 6679.
31 S. Das, A. Sirohi, G. Kumar Gupta, S. Kamboj, A. Vasdev, S. Gayen, P. Guptasarma, T. Das and G. Sheet, *Phys. Rev. B*, 2018, **97**, 235306.
32 A. V. Matetskiy, V. V. Mararov, I. A. Kibirev, A. V. Zotov and A. A. Saranin, *J. Condens. Matter Phys.*, 2020, **32**, 165001.
33 P. Hohenberg and W. Kohn, *Phys. Rev.*, 1964, **136**, B864.
34 G. Kresse and J. Furthmüller, *Comput. Mater. Sci.*, 1996, **6**, 15.
35 J. P. Perdew, A. Ruzsinszky, G. I. Csonka, O. A. Vydrov, G. E. Scuseria, L. A. Constantin, X. Zhou and K. Burke, *Phys. Rev. Lett.*, 2008, **100**, 136406.
36 J. P. Perdew, A. Ruzsinszky, G. I. Csonka, O. A. Vydrov, G. E. Scuseria, L. A. Constantin, X. Zhou and K. Burke, *Phys. Rev. Lett.*, 2009, **102**, 039902.
37 J. P. Perdew and A. Zunger, *Phys. Rev. B: Condens. Matter Mater. Phys.*, 1981, **23**, 5048.
38 S. Grimme, *J. Comput. Chem.*, 2006, **27**, 1787.
39 H. J. Monkhorst and J. D. Pack, *Phys. Rev. B: Solid State*, 1976, **13**, 5188.
40 F. D. Murnaghan, *Proc. Natl. Acad. Sci. U. S. A.*, 1944, **30**, 244.
41 F. Birch, *Phys. Rev.*, 1947, **71**, 809.
42 A. Togo, F. Oba and I. Tanaka, *Phys. Rev. B: Condens. Matter Mater. Phys.*, 2008, **78**, 134106.
43 L. Chaput, A. Togo, I. Tanaka and G. Hug, *Phys. Rev. B: Condens. Matter Mater. Phys.*, 2001, **84**, 094302.
44 J. Skelton, L. Burton, A. Jackson, F. Oba, S. Parker and A. Walsh, *Phys. Chem. Chem. Phys.*, 2017, **19**, 12452.
45 J. M. Skelton, Phonopy-spectroscopy, **https://github.com/JMSkelton/Phonopy-Spectroscopy**.
46 A. Togo, L. Chaput and I. Tanaka, *Phys. Rev. B: Condens. Matter Mater. Phys.*, 2015, **91**, 094306.
47 Y. Page and P. Saxe, *Phys. Rev. B: Condens. Matter Mater. Phys.*, 2002, **65**, 104104.
48 R. Gaillac, P. Pullumbi and F.-X. Coudert, *J. Phys.: Condens. Matter*, 2016, **28**, 275201.
49 H. Koc, A. M. Mamedov, E. Deligoz and H. Ozisik, *Solid State Sci.*, 2012, **14**, 1211.
50 N. Kuganathan, *E-J. Chem.*, 2009, **6**, S147.
51 V. L. Deringer, R. P. Stoffel, M. Wuttig and R. Dronskowski, *Chem. Sci.*, 2015, **6**, 5255.
52 G. P. Voutsas, A. G. Papazoglou, P. J. Rentzeperis and D. Siapkas, *Z. Kristallogr.*, 1985, **171**, 261.
53 T. B. Nasr, H. Maghraoui-Meherzi, H. Abdallah and R. Bennaceur, *Physica B*, 2011, **406**, 287.
54 Y. Liu, K. Chua, T. C. Sum and C. Gan, *Phys. Chem. Chem. Phys.*, 2013, **16**, 345.
55 L. Lundegaard, R. Miletich, T. Balic-Zunic and E. Makovicky, *Phys. Chem. Miner.*, 2003, **30**, 463.
56 I. Efthimiopoulos, C. Buchan and Y. Wang, *Sci. Rep.*, 2016, **6**, 24246.

57 P. Bayliss and W. Nowacki, *Z. Kristallogr. - Cryst. Mater.*, 2015, **135**, 308.
58 A. Kyono, M. Kimata, M. Matsuhisa, Y. Miyashita and K. Okamoto, *Phys. Chem. Miner.*, 2002, **29**, 254.
59 H. Koc, H. Ozisik, E. Deligöz, A. M. Mamedov and E. Ozbay, *J. Mol. Model.*, 2014, **20**, 2180.
60 E. Zahedi and B. Xiao, *Comput. Mater. Sci.*, 2015, **101**, 301.
61 L. Lundegaard, E. Makovicky, T. Ballaran and T. Balic-Zunic, *Phys. Chem. Miner.*, 2005, **32**, 578.
62 I. Efthimiopoulos, J. Kemichick, X. Zhou, S. Khare, D. Ikuta and Y. Wang, *J. Phys. Chem. A*, 2014, **118**, 1713.
63 J. J. Carey, J. P. Allen, D. O. Scanlon and G. W. Watson, *J. Solid State Chem.*, 2014, **213**, 116.
64 Y. Wang, M. Yanmei, G. Liu, J. Wang, Y. Li, Q. Li, J. Zhang, Y. Ma and G. Zou, *Sci. Rep.*, 2018, **8**, 14795.
65 C. Li, J. Zhao, Q. Hu, Z. Liu, Z. Yu and H. Yan, *J. Alloys Compd.*, 2016, **688**, 329.
66 A. E. Mattsson, R. Armiento, J. Paier, G. Kresse, J. M. Wills and T. R. Mattsson, *J. Chem. Phys.*, 2008, **128**, 084714.
67 R. Armiento and A. E. Mattsson, *Phys. Rev. B: Condens. Matter Mater. Phys.*, 2005, **72**, 085108.
68 A. E. Mattsson and R. Armiento, *Phys. Rev. B: Condens. Matter Mater. Phys.*, 2009, **79**, 155101.
69 D. Fan, J. Xu, J. Liu, Y. Li and H. Xie, *High Temp. – High Pressures*, 2014, **43**, 351.
70 M. Sternik and K. Parlinski, *J. Chem. Phys.*, 2005, **123**, 204708.
71 E. L. da Silva, J. M. Skelton, S. C. Parker and A. Walsh, *Phys. Rev. B: Condens. Matter Mater. Phys.*, 2015, **91**, 144107.
72 M. Born, *Proc. Cambridge Philos. Soc.*, 1940, **36**, 160.
73 M. T. Dove, *Introduction to Lattice Dynamics*, Cambridge University Press, 1993.
74 M. T. Dove, *Structure and Dynamics: An Atomic View of Materials, Oxford Master Series in Physics*, 2003.
75 M. T. Dove, *Am. Mineral.*, 2015, **82**, 213.
76 G. Venkataraman, *Bull. Mater. Sci.*, 1979, **1**, 129.
77 M. Di Gennaro, S. Saha and M. Verstraete, *Phys. Rev. Lett.*, 2013, **111**, 025503.
78 B. B. Karki, G. J. Ackland and J. Crain, *J. Phys.: Condens. Matter*, 1997, **9**, 8579.
79 F. Mouhat and F.-X. Coudert, *Phys. Rev. B: Condens. Matter Mater. Phys.*, 2014, **90**, 224104.
80 S. Pfeiffer, PhD thesis, Universität Stuttgart, 2009.
81 F. J. Manjón, R. Vilaplana, O. Gomis, E. Pérez-González, D. Santamaría-Pérez, V. Marín-Borrás, A. Segura, J. González, P. Rodríguez-Hernández, A. Muñoz, C. Drasar, V. Kucek and V. Muñoz Sanjosé, *Phys. Status Solidi B*, 2013, **250**, 669.
82 R. Vilaplana, D. Santamaría-Pérez, O. Gomis, F. J. Manjón, J. González, A. Segura, A. Muñoz, P. Rodríguez-Hernández, E. Pérez-González, V. Marín-Borrás, V. Muñoz Sanjose, C. Drasar and V. Kucek, *Phys. Rev. B: Condens. Matter Mater. Phys.*, 2011, **84**, 184110.
83 R. Vilaplana, S. G. Parra, A. Jorge-Montero, P. Rodríguez-Hernández, A. Munoz, D. Errandonea, A. Segura and F. J. Manjón, *Inorg. Chem.*, 2018, **57**, 8241.
84 R. Vilaplana, O. Gomis, F. J. Manjón, H. M. Ortiz, E. Pérez-González, J. López-Solano, P. Rodríguez-Hernández, A. Muñoz, D. Errandonea, V. V. Ursaki and I. M. Tiginyanu, *J. Phys. Chem.*, 2013, **117**, 15773.
85 V. P. Cuenca-Gotor, J. A. Sans, J. Ibáñez, C. Popescu, O. Gomis, R. Vilaplana, F. J. Manjón, A. Leonardo, E. Sagasta, A. Suárez-Alcubilla, I. G. Gurtubay, M. Mollar and A. Bergara, *J. Phys. Chem.*, 2016, **120**, 19340.
86 G. P. Lindberg and B. A. Weinstein, *Phys. Rev. B*, 2016, **94**, 134102.
87 F. J. Manjón, S. Gallego-Parra, P. Rodríguez-Hernández, A. Muñoz, C. Drasar, V. Muñoz-Sanjosé and O. Oeckler, *J. Mater. Chem. C*, 2021, **9**, 6277.
88 R. Wang, F. R. L. Lange, S. Cecchi, M. Hanke, M. Wuttig and R. Calarco, *Adv. Funct. Mater.*, 2018, **28**, 1705901.
89 J. Wilson and A. Yoffe, *Adv. Phys.*, 1969, **18**, 193.
90 Y. Cheng, O. Cojocaru-Mirédin, J. Keutgen, Y. Yu, M. Küpers, M. Schumacher, P. Golub, J.-Y. Raty, R. Dronskowski and M. Wuttig, *Adv. Mater.*, 2019, **31**, 1904316.
91 H. Cheng, J. Zhang, Y. Li, G. Li and X. Li, *J. Appl. Phys.*, 2017, **121**, 225902.
92 J. A. Sans, R. Vilaplana, E. L. da Silva, C. Popescu, V. P. Cuenca-Gotor, A. Andrada-Chacón, J. Sánchez-Benitez, O. Gomis, A. L. J. Pereira, P. Rodríguez-Hernández, A. Muñoz, D. Daisenberger, B. García-Domene, A. Segura, D. Errandonea, R. S. Kumar,. Oeckler, P. Urban, J. Contreras-García and F. J. Manjón, *Inorg. Chem.*, 2020, **59**, 9900.
93 C. Morin, S. Corallini, J. Carreaud, J.-B. Vaney, G. Delaizir, J.-C. Crivello, E. B. Lopes, A. Piarristeguy, J. Monnier, C. Candolfi, V. Nassif, G. J. Cuello, A. Pradel, A. P. Goncalves, B. Lenoir and E. Alleno, *Inorg. Chem.*, 2015, **54**, 9936.
94 S. Nakajima, *J. Phys. Chem. Solids*, 1963, **24**, 479.
95 A. Adam, *Mater. Res. Bull.*, 2007, **42**, 1986–1994.
96 T. L. Anderson and H. B. Krause, *Acta Crystallogr., Sect. B: Struct. Crystallogr. Cryst. Chem.*, 1974, **30**, 1307.
97 L. Vereshchagin, E. Itskevich, E. Atabaeva and S. Popova, *Fiz. Tverd. Tela*, 1965, **6**, 2223.
98 E. Atabaeva, N. Bendeliani and S. Popova, *Fiz. Tverd. Tela*, 1973, **75**, 3508.
99 E. Y. Atabaeva, S. A. Mashkov and S. V. Popova, *Kristallografiya*, 1973, **18**, 173.
100 L. Lityagina, L. Kulikova, I. Zibrov, T. Dyuzheva, N. Nikolaev and V. Brazhkin, *J. Alloys Compd.*, 2015, **644**, 799.
101 V. A. Kirkinsky, A. P. Ryaposov and V. G. Yakushev, in *Chalcogenides of As, Sb and Bi under High Pressures*, Novosibirsk: Nauka, 1985, p. 108.
102 V. A. Kirkinsky, A. P. Ryaposov and V. G. Yakushev, *Fiz. Tverd. Tela*, 1969, **11**, 2382.
103 A. M. Ganose, A. J. Jackson and D. O. Scanlon, *J. Open Source Softw.*, 2018, **3**, 717.
104 X. Hong, M. Newville, Y. Ding, D. Zhang, T. Irifune, G. Gu and H.-K. Mao, *Phys. Rev. B*, 2020, **102**, 134110.
105 X. Hong, M. Newville, Y. Ding, D. Zhang, T. Irifune, G. Gu and H.-K. Mao, *Phys. Rev. B*, 2020, **101**, 214107.

 